Chapter 3

Oxygen vacancy modulated TiO$_2$ nanostructures for efficient detection of VOCs

3.1 Introduction

The crucial characteristic determining the nature of material is dimensionality: the same alloy displays totally unique properties depending upon whether it is synthesized in 0-D, 1-D, 2-D and 3-D [1]. TiO$_2$ has an advantage of being synthesized in 1-D nanotubes and 0-D nanoparticles. Both the nanoforms (0-D and 1-D) have unique properties that are utilized for various applications including gas or vapor sensing [2]. TiO$_2$ nanotubes and nanoparticles composites with other nanomaterial exhibits amazing properties and acts as a building block of the formed nanocomposite [3].

TiO$_2$ nanostructures have been widely utilized to detect variety of volatile organic compounds (VOCs) in industry, food, biomedical, environmental, traffic safety, indoor safety applications etc [4]. The above applications require reliable VOC sensor with application specific selectivity, low power operation, highly stable and applicable for very high dynamic range of detection [5]. To fulfil the above requirements, numerous methods have been adopted to improve the performance of a nanostructured metal oxides. One of the methods is to dope the metal oxide with impurities [6],[7]. But, most of the time, the doping with external impurities in metal oxide are non-uniform in nature and the doped metal oxide exhibits poor repeatability [8]. The poor repeatability issue is observed for the metal oxide nanocomposites sensors also [9-11].

One of the ways to enhance the sensing performance of metal oxides is to increase or decrease the oxygen vacancy in nanoscale metal oxides which can be considered 'self-doping'. Many reports have been published regarding the increase of sensor performance by increasing the number of oxygen vacancies in metal oxides. SnO$_2$ nanocrystals with abundant oxygen vacancies for room temperature NO$_2$ sensing have been reported by Wei and group [12]. Wang and co-workers demonstrated high-performance gas sensing achieved by mesoporous tungsten oxide mesocrystals with increased oxygen vacancies [13]. Synthesis and oxygen vacancy related NO$_2$ gas sensing properties of ZnO:Co nanorods arrays gown by a hydrothermal method has been described by Zou and group [14]. Wu and workers reported Al-doping induced formation of oxygen-vacancy for enhancing gas-sensing properties of SnO$_2$ nanotubes by

electrospinning [15]. Room temperature alcohol sensing by oxygen vacancy controlled TiO_2 nanotube array has been reported by Hazra and group [16],[17]. Yu and co-workers described both oxygen vacancies defects and porosity facilitated NO_2 gas sensing response in 2-D ZnO nanowalls at room temperature [18]. So, these reports confirm the potential of oxygen vacancy modulation in nanoforms metal oxide for enhanced gas/VOC sensing.

On the other hand, 0-D TiO_2 nanoparticles have gained much attention in industry and academia. Huge surface area of nanoparticles aggregates with high electron transfer rate makes them popular for VOC sensing also [19].

Teleki and group had demonstrated sensing of organic vapours by TiO_2 nanoparticles synthesized via flame spray pyrolysis method. They showed the sensing of acetone, isoprene and ethanol at 500 °C in dry N_2 and O_2 [20]. Arafat and coworkers demonstrated ethanol sensing by TiO_2 nanoparticles. They depicted a high sensitivity towards ethanol than H_2 and CH_4 at 600 °C with a response and recovery time of 3 min and 15 min respectively [21]. Rella and group reported ethanol and acetone sensing by TiO_2 nanoparticles film that was deposited using matrix assisted pulsed laser evaporation. They achieved a response magnitude of 12 % and 6 % to 100 ppm of ethanol and acetone at 350 °C and 400 °C respectively [22]. Pandeeswari and group fabricated TiO_2 nanoparticles by sol gel method and tested towards ethanol vapours at 30 °C. They depicted a response magnitude of 535 % with quick response/ recovery time (5 s/52 s) to 50 ppm of ethanol [23].

This chapter describes the two different nanostructures of TiO_2 for efficient VOC sensing. 1-D TiO_2 nanotubes prepared via electrochemical anodization were further subjected to cathodization and chemical reduction for oxygen vacancy modulation. All the nanotube samples with various self-doping levels were transformed to the Au/TiO_2 nanotube/Ti type sandwich structured sensor devices and tested in the exposure of 100 ppm of ethanol in air. 0-D undoped TiO_2 nanoparticles fabricated via solgel method were fabricated in planar device structure. TiO_2 nanoparticles based planar device structure sensor was tested against different groups of VOCs.

3.2 Oxygen vacancy modulated TiO_2 nanotubes

3.2.1 Synthesis

The detailed electrochemical anodization method, used to prepare the TiO_2 nanotube array is discussed in section 2.2.1 of chapter 2. Further two separate methods, i.e. (i) electrochemical cathodization and (ii) chemical reduction, were used to modulate the oxygen vacancy level in

the TiO_2 nanotubes. Sample S_0 was taken as the base TiO_2 nanotubes without any further reduction.

Electrochemical cathodization

Two TiO_2 nanotube samples (S_1 and S_2) were reduced by a potentiostatic cathodization route where 1 M sodium sulfate (Na_2SO_4) aqueous solution was used as the electrolyte. An annealed TiO_2 nanotube/Ti sample (i.e.S_0) was used as the anode and the rectangular-shaped graphite sheet was used as the cathode. S_1 and S_2 samples were prepared at different potentials of -1.0 V and -1.5 V for a polarization period of three seconds (3 s). After cathodization, both samples (i.e. S_1 and S_2) were washed with water and ethanol and then dried in air at 100 °C for one hour.

Chemical reduction

Another two samples (S_3 and S_4) of TiO_2 nanotubes were prepared with a chemical reduction method where hydrazine hydrate (N_2H_4) was used as the reducing agent. Annealed TiO_2 nanotube samples were placed in the hydrazine hydrate solution for 5 hours and heated at 85 °C and 115 °C for S_3 and S_4 samples, respectively. After five hours of hydrazine hydrate treatment, both samples were cleaned with Milli-Q water and then ethanol and dried in air at 100 °C for one hour.

3.2.2 Characterizations

Morphological characterization

No deformation or morphology changes were observed in the scanning electron micrographs after reduction of TiO_2 nanotubes by cathodization and chemical reduction routs. FESEM image and TEM are similar as depicted in Fig. 2.1. However, the post-anodization treatment for the variation of oxygen vacancy had no effect on the surface morphology of the TiO_2 nanotubes for all the samples.

Structural characterization

The crystallinity of TiO_2 nanotubes were revealed by XRD (Fig. 3.1(a-e)). The sharp and high intensity peak at 24.5° describes the anatase phase of TiO_2 nanotubes having crystallinity (101) in all the samples (S_0-S_4). Low intensity anatase peaks of (200) and (118) at 47.27° and 62.28° were observed in all the reduced samples (S_1- S_4). All the peaks labelled as T at 29.64°, 34.1°, 36.9°, 39.2°, 52°, 69.9° correspond to substrate-titanium. The small peaks at 53.2° and 54.1° correspond to the anatase (105) and (211) respectively in sample S_0 and S_3 only (Fig. 3.1(a) and (d).). Most interestingly, rutile (110) crystallinity peak at 27.4° was observed for cathodic

reduction samples as shown in Fig. 3.1(b) and (c). The XRD peaks for anatase and rutile TiO_2 was authenticated by JCPDS file No. 21-1272 and 21-1276 respectively. However, the formation of anatase (101) major for all the TiO_2 nanotubes is a good agreement with TEM image shown in Fig. 2.1(d) and (e).
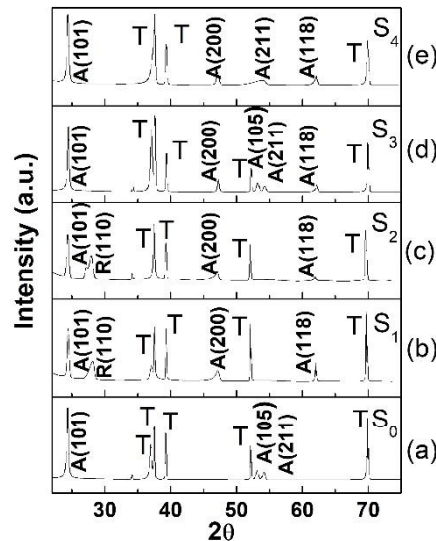

Fig. 3.1. XRD spectra of five different TiO_2 nanotubes with different level of reductions i.e. (a) S_0 (as grown); (b) S_1 (reduction by cathodization at -1.0 V); (c) S_2 (reduction by cathodization at -1.5 V); (d)S_3 (chemical reduction at 85°C); (e) S_4 (chemical reduction at 115°C).
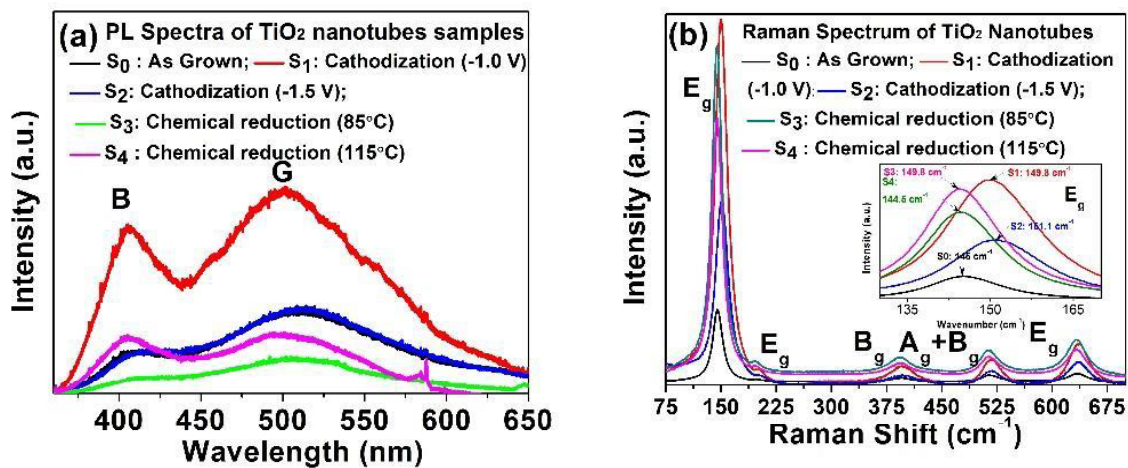

Fig. 3.2. Characterizations to estimate the amount of reduction in TiO_2 nanotubes array with respect to pure TiO_2 nanotubes array: (a) PL spectra; (b) Raman spectra.

Spectroscopic characterizations were carried out to estimate the level of non-stiochiometery of TiO_2 nanotubes. Both PL and Raman spectra were collected for all the TiO_2 nanotube array samples (S_0-S_4) and shown in Fig. 3.2(a) and 3.2(b), respectively.

Photoluminescence (PL) spectroscopy is an important characterization tool to study the defects related with the metal oxides. Various reduction level of TiO_2 nanotube samples was estimated

qualitatively comparing the recorded PL spectra under 325 nm excitation wavelength at room temperature (300 K) as shown in Fig. 3.2(a). PL spectra showed two main peaks; one in the UV region that was centered at ~404 nm and the second one in green region centered at ~510 nm. The first peak represents the band-to-band emission i.e. the electronic transition from conduction band to valance band [24]. This peak represents the band gap of TiO_2 nanotubes around 3.2 eV [25]. The second peak in green region is originated due to the oxygen vacancies (defects) related trap assisted recombination [26-30]. In current study, relative quantity of oxygen vacancy was estimated by considering two main observations in Fig.3.2(a) i.e. (i) shift of band-to-band emission peak (B) which indicates the bandgap of the TiO_2 nanotubes and (ii) intensity ratio of defect peak (G) and band-to-band emission (B) peak or I_G/I_B.

Position of peak-B and I_G/I_B are summarized in Table 3.1 for all the five samples (S_0-S_4). A small right shift for S_1 and significant right shift for S_2, S_3 of peak-B as comparing with S_0 sample indicate the relative increment of self-doping in term of oxygen vacancy and reduction of band gap. As compared to the S_0, no shift of peak-B was observed for S_4. Quite a high I_G/I_B was calculated for S_2 (1.81) and S_3 (1.73) which indicated the high level reduction TiO_2 nanotubes. Considering S_0 (I_G/I_B=1.18) as the reference, a moderate level of reduction was observed for S_1 (I_G/I_B=1.28) and almost no reduction was observed for S_4 (I_G/I_B=1.06).

Table 3.1 Depicting the shifts in PL and Raman spectroscopy of all the reduced TiO_2 nanotubes array with respect to pure TiO_2 nanotubes array.

Sample	Photoluminescence		Raman Spectroscopy	
	B	I_G/I_B	Eg	FWHM
S_0	405.4	1.18	145	17.26
S_1	407	1.28	149.8	24
S_2	417	1.81	151.1	24.5
S_3	415	1.73	149.8	19.84
S_4	405	1.06	144.5	16.38

Raman spectroscopy is an important tool to study the composition of materials. Raman spectra of all the TiO_2 nanotube array samples were recorded at 532 nm laser at room temperature (Fig.3.2 (b)). Five peaks were observed for all the TiO_2 nanotubes samples. The active modes present nearly at 145 cm^{-1} (E_g), 195.4 cm^{-1} (E_g), 395.2 cm^{-1} (B_g), 514.6 cm^{-1} (A_g+B_g) and 634.4 cm^{-1} (E_g) corresponds to the anatase phase of TiO_2 [31-35]. In current study, level of oxygen vacancy in TiO_2 nanotube samples was estimated with (i) blue shift and (ii) broadening or full-

width half maxima (FWHM) of E_g peak near 145 cm^{-1}. Due to creation of oxygen vacancy, oxygen atoms are removed from TiO_2 lattice reducing the bond-length of Ti-O and it results in the right shift of E_g peak towards the higher wavenumber and increases the FWHM [31],[36],[37]. The measured and calculated position and FWHM of E_g peak for five different samples are represented in Table 1. A significant right shift of E_g peak was observed for S_1, S_2 and S_3 sample compared to the S_0 where S_1 showed maximum shift of 6.1 cm^{-1} (151.1-145 cm^{-1}). No significant blue shift was observed for S_4 as compared to the S_0 (Table 3.1). Broadening E_g peak was significant in case of S_1 and S_2 and moderate for S_3 where as S_4 showed almost no such broadening (Table 3.1). The Raman spectroscopy results showed a good agreement with PL spectroscopy results confirming the highest reduction level for S_2 followed by S_1 and S_3 and almost no significant reduction for S_4.

Chemical characterization

Table 3.2 Summary of de-convoluted fit-peak position and area of XPS O(1s) peak for S_0 to S_4

Sample	Fit Peak 1 (P1)		Fit Peak 2 (P2)		$\dfrac{A_{P2}}{A_{P1} + A_{P2}}$	$\dfrac{A_{P2}}{A_{P1} + A_{P2}} \times 100$
	Position (eV)	Area (A_{P1})	Position (eV)	Area (A_{P2})		
S_0	530.71	18544	532.13	6180	0.2499	24.99%
S_1	530.52	19480	532.03	6921	0.2621	26.21%
S_2	530.40	17886	531.89	9247	0.3408	34.08%
S_3	530.40	17174	531.99	9822	0.3638	36.38%
S_4	530.44	18040	531.71	8943	0.3314	33.14%

X-ray photoelectron spectra (XPS) of five different TiO_2 nanotubes array (S_0-S_4) were recorded to study the possibility of the formation of sub-oxidation states like Ti^{3+} and Ti^{2+} which might be originated due to the creation of oxygen vacancies [38][39]. High intensity binding energy Ti2p peaks for S_0-S_4 was recorded with high resolution scan to observe the shift of doublet peaks i.e. Ti2p$_{3/2}$ and Ti2p$_{1/2}$ (Fig. 6(a)). Ti2p$_{3/2}$ peak location was found from Fig. 3.3(a) as 459.5 eV, 459.36 eV, 459.18 eV, 459.25 eV and 459.27 eV for S_0, S_1, S_2, S_3 and S_4, respectively (inset of Fig. 3.3(a)). As compared to S_0, Ti2p$_{3/2}$ peak shift is maximum for S_2 and gradually decreasing for S_2, S_3 and S_4. These results confirm the availability of T^{3+} and T^{2+} oxidation states of Ti_2O_3 and TiO_2 is maximum for S_2 and gradually decreasing for S_2, S_3 and S_4. As the penetration depth of the emitted photo electrons is very small (even a few nanometre), the sub-

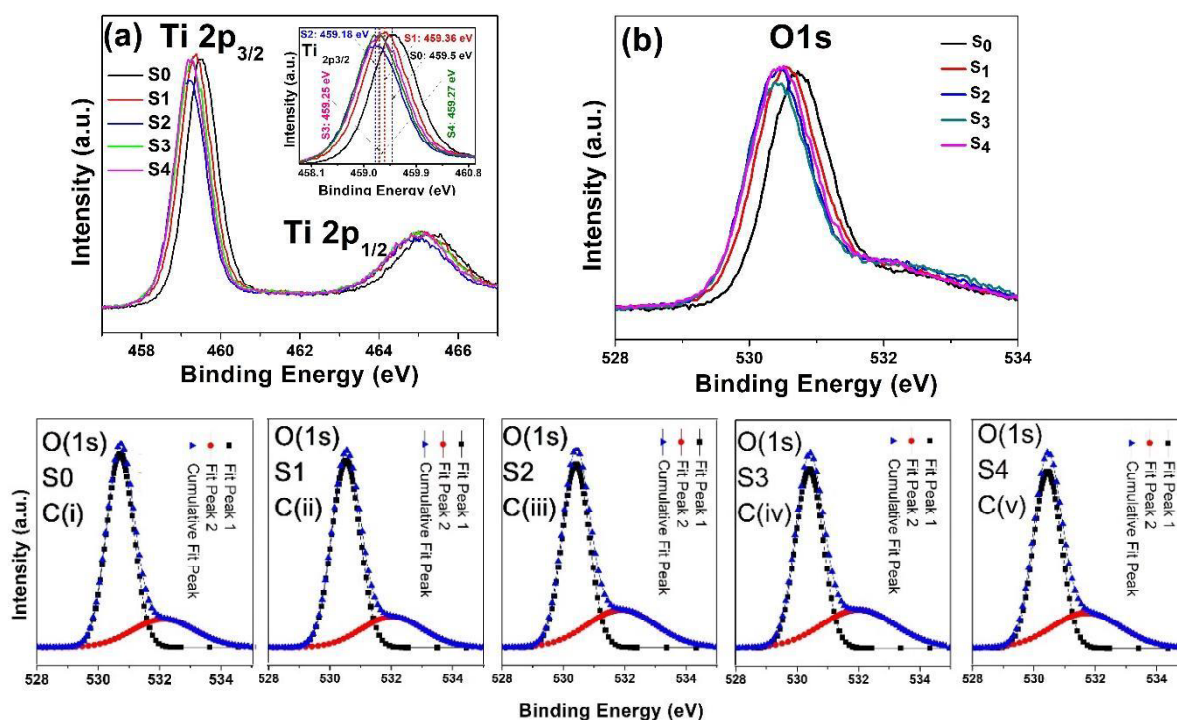oxide formation can consider majorly from the nanotube surface excepting the Ti/TiO$_2$ interface.

Fig. 3.3. High resolution XPS spectra of TiO$_2$ nanotube array of different level of reduction; (a) Ti2p peak and (b) O1s peak.

Fig. 3.3(b) shows the high resolution O1s spectra of S$_0$ to S$_4$ samples. Two binding energy peaks near 530 eV (peak 1) and 532 eV (peak 2) are visible for all the TiO$_2$ nanotube samples (Fig. 3.3(b)) where peak 1 corresponds chemically bonded lattice oxygen (Ti-O) and peak 2 corresponds physiosorbed weakly bonded surface oxygen species or hydroxyl groups [38],[40]. In current study, O1s peak (Fig. 3.3(b)) was de-convoluted in peak 1 (530 eV) and peak 2 (532 eV) to estimate the amount of surface and bulk oxygen of TiO$_2$ nanotubes with different level of reduction. Fig. 3.3(c(i-v)) represents the de-convolution peak1 and 2 for S$_0$ to S$_4$ nanotubes. Position and area of fit-peak 1 and 2 for S$_0$ to S$_4$ are summarized in Table 3.2. For S$_0$ to S$_4$, fit-peak 1 and 2 were located in-between 530.4 to 530.71 eV and 532.13 to 532.71 eV respectively. To get a relative approximation of surface oxygen over total oxygen of TiO$_2$ nanotube samples, the ratio of the area of fit-peak 2 (A$_{P2}$) and total area of fit-peak 1 and 2 (A$_{P1}$+ A$_{P2}$) was taken for S$_0$ to S$_4$ and represented in Table 3.2. Due to having a significantly high surface area, overall surface oxygen was found to be very high in case of all the TiO$_2$ nanotube samples. Among all the reduced TiO$_2$ nanotubes, S$_3$ showed the maximum amount of surface oxygen as 36.38%

when as-grown TiO_2 nanotubes (i.e. S_0) showed 24.99% of surface oxygen. Surface oxygen was also calculated quite high in case of S_2 (34.08%) and S_4 (33.14%) samples.

After considering all the results of three spectroscopic studies i.e. photoluminescence, Raman and X-ray photoelectron spectroscopy, we can accomplish that successful reduction was possible in both the reduction techniques. Both the samples by cathodic reduction (S_1 and S_2) showed significant amount of self-doping and most of the cases S_2 exhibited highest level of reduction among all the five TiO_2 nanotubes. Chemically reduced S_3 represented significant reduction when almost no reduction was observed for S_4 compared to the reference sample (S_0).

3.2.3 Device fabrication

Gold top-electrode was deposited on TiO_2 nanotubes/Ti samples for sensor fabrication. Five metal-insulator-metal (MIM) structured sensors with Au top electrode, Ti bottom electrode and TiO_2 nanotube as the sensing layer (S_0-S_4) were fabricated for the detection of volatile organic compounds (VOCs). The samples were enfolded in aluminium masks having a total of four openings of 2 mm $\times$ 2 mm each for top electrode formation, separated by a distance of 2 mm. Au was deposited using electron beam deposition technique. The Au deposited with a thickness of ~100 nm on the sample was taken as the top electrode and Ti substrate was taken as the bottom electrode (Fig 3.4). The bottom electrode was created by selective etching the TiO_2 nanotube array from one corner of the sample with HF.
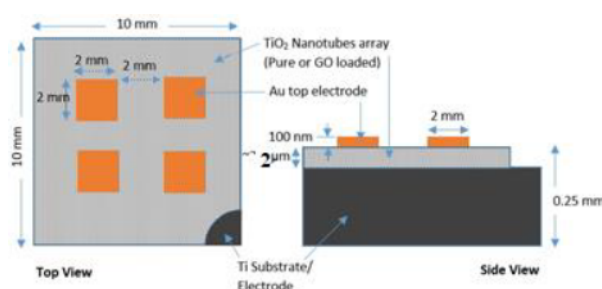

Fig. 3.4. Top and side view of sensor device structure with dimensions.

3.2.4 VOC sensing

All the fabricated sensors were tested under different VOCs at different temperatures (50 ℃, 100 ℃, 150 ℃ and 200 ℃). The sensor setup consisted of three glass chambers i.e. (i) sensing chamber to place the sensor, (ii) mixing chamber to dilute the vapor by synthetic air to maintain required concentration and (iii) vapor generation chamber. The schematic of the sensor characterization setup is shown in Fig.3.5. All the chambers were placed inside a heating

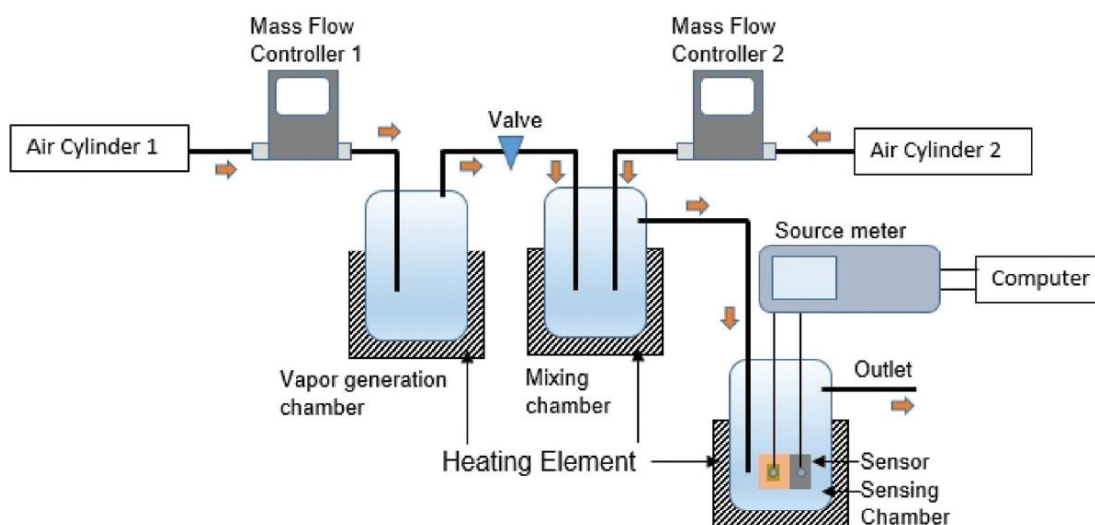mantle to maintain appropriate temperature. The flow of air was maintained with mass flow controllers (MFCs).

Fig. 3.5. Schematic of the sensor characterization setup to detect volatile organic compounds (VOCs) of different concentrations.

Au/TiO$_2$ nanotubes/Ti - sandwich structure sensor with five self-doped TiO$_2$ nanotubes (S$_0$-S$_4$) were tested at four different temperatures i.e. 50 °C, 100 °C, 150 °C and 200 °C on the exposure of 100 ppm of ethanol (test) vapours in air. All the sensors were operated at a constant DC bias of 0.5 V (Keithley 6487). Initial performance of all the five sensors was compared with three sensing parameters i.e. response magnitude, response time and recovery time as a function of operating temperature (50-200 °C) as shown in Fig. 3.6(a), (b) and (c)). Response magnitude was measured as $[(R_a-R_g)/R_a]\times100$ % where R_a is the resistance in air and R_g is the resistance in exposure to vapor. Response and recovery time was measured as time taken by the sensor to reach 90% of maximum change in the exposure to target vapour.
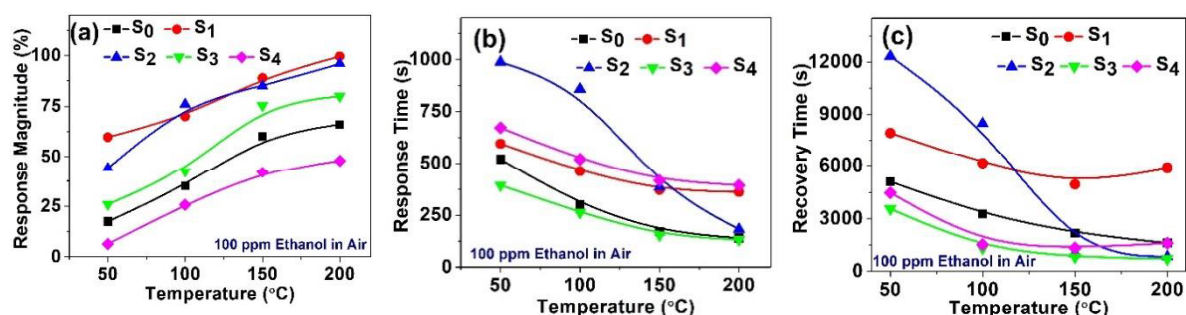

Fig. 3.6. (a) Response magnitude, (b) response time, (c) recovery time, as a function of temperature in 100 ppm of ethanol.

Self-doping due to incremental oxygen vacancy have significant influence to lower the operating temperature of a metal oxide sensor as discussed in our earlier report [17].

S_1 and S_2 nanotubes synthesized by cathodic reduction showed very high response throughout the temperature range (50°C -200°C). S_1 and S_2 exhibited 60% and 44% response at 50°C and 99% and 96% at 200°C. Chemically reduced S_3 showed third highest response (26% at 50°C and 80% at 200°C) and S_4 showed lowest response (smaller than S_0) i.e. 6% at 50°C and 47% at 200°C. Every sensor showed the highest response magnitude at 200°C and the lowest response magnitude at 50°C. All the sensors attributed a linear increment from 50°C to 150°C and a saturation tendency in-between 150°C to 200°C (Fig.3.6(a)).
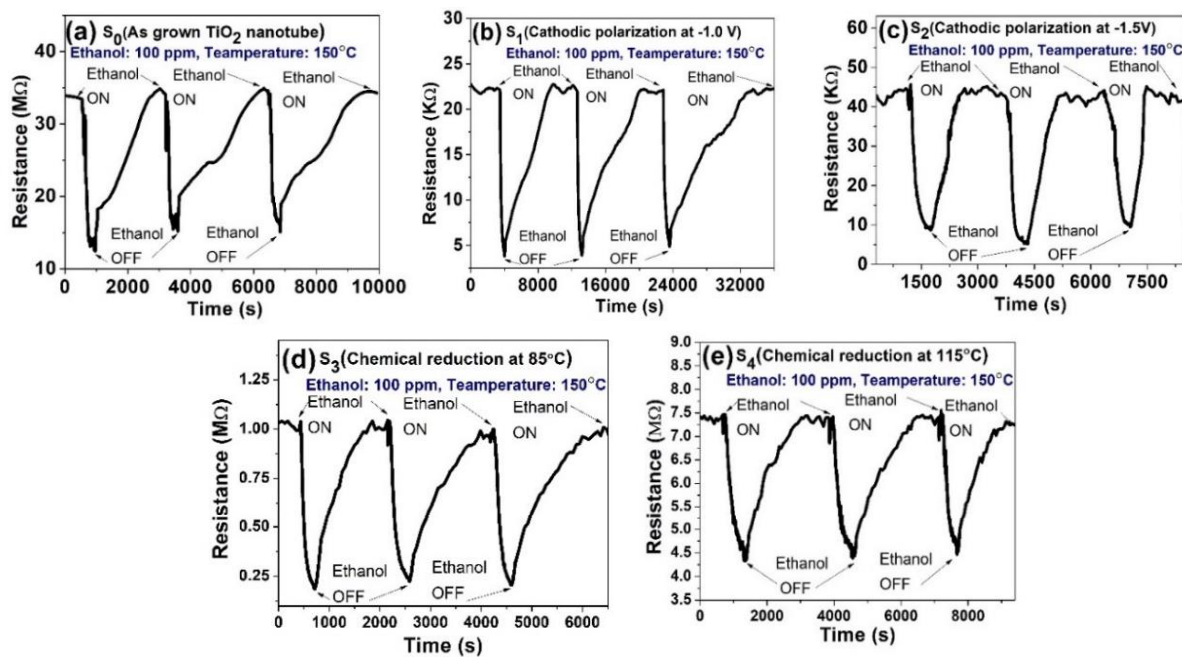

Fig. 3.7. Stability test of (a) S_0; (b) S_1; (c) S_2;(d) S_3;(e) S_4; at 150 °C for 100 ppm of ethanol.

The response and recovery time principally depend upon the time required by the VOC molecules to get adsorbed and desorbed on the surface of the sensing layer respectively. At high operating temperature, due to availability of sufficient energy, dissociation, surface adsorption and desorption become faster resulting in a quick response and recovery of all the sensors (Fig. 3.6(b) and (c)). Sensors S_1 and S_2 with high amounts of self-doping provided highest sensitivity at all the temperatures. But it took a longer time than usual for these sensors to achieve maximum change (response) and return to the original resistance (recovery) because of the presence of large amounts of interaction sites in the nanotubes. At very low temperature, response and recovery both took extremely long time for S_1 and S_2 samples as shown in Fig. 3.6(b) and (c). Most importantly, S_3 (chemical reduction) sensor possibly attribute an optimized level of reduction in TiO_2 nanotubes array offering lowest response (155 s at 150°C) and

recovery (779 s at 150°C) time at all operating temperatures (50-200°C). After studying the sensor performance in Fig. 3.6, 150°C was considered an optimized temperature for all the sensors because the response magnitude, response time and recovery time became saturated above 150°C. So, the repeated cycle characteristics of five sensors are represented at 150°C in Fig. 3.7 (a-e).

Two common observations were made for all the sensing devices tested in exposure to ethanol vapours. First the resistance was decreased with increase in temperature and the response magnitude for all the sensors was increased with increase in temperature. Base line resistance was measured in mega-ohm range for S_0 (35 MΩ), S_4 (7.5 MΩ), S_3 (1.1 MΩ) whereas kilo-ohm range resistance was observed for S_1 (22 kΩ) and S_2 (40 kΩ) at 150°C. The baseline resistance can also give an estimate about the self-doping level of the five different TiO_2 nanotubes and in the present study the baseline resistance of the sensors exhibited a good agreement with the spectroscopy characterization results. However, a small fraction of the resistance can also change based on the quality of the metal (Au)/TiO_2 junctions. All the sensors showed a stable and repeatable response with stable baseline resistance at 150°C. So, the overall performance confirms that S_1 and S_2 sensors have high sensitivity and can sense VOCs at 50°C even at room temperature (25°C). Though the response magnitude was moderate, owing to the fastest response and recovery time, S_3 sensor was considered to show other detailed sensing performances like transient response varying the dynamic range of ethanol from 20 ppm to 300 ppm (Fig.3.8(a)), single pulse response at different temperatures (Fig. 3.8(b)) and cross-sensitivity study of the sensor in the exposure of 100 ppm of other VOCs like Benzene, Xylene, 2-propanol and Acetone at 150°C (Fig. 3.8(c)).
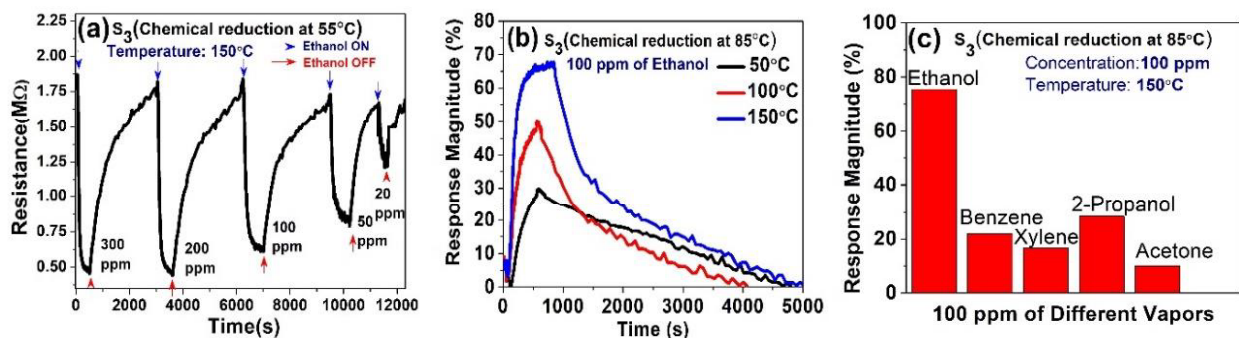

Fig. 3.8. Sensing performance of chemically reduced S_3 sensor; (a) transient behaviour (20 to 300 ppm); (b) resistive response magnitude at different temperatures (50 °C, 100 °C, 150 °C); (c) cross sensitivity of ethanol comparing with Benzene, Xylene, 2-propanol and Acetone of 100 pm concentration at 150 °C.

Promising transient behaviour was observed for S_3 sensors under the ethanol concentration range of 20 ppm to 300 ppm. Almost similar responses at 200 ppm and 300 ppm confirmed the saturating tendency of the sensor beyond 200 ppm (Fig. 3.8(a)). Single pulse measurement at three different temperatures (50 ℃, 100 ℃, 150 ℃) clearly shows the increment response and recovery time with decrease of operating temperature (Fig. 3.8(b)). Finally, the S_3 showed its selective nature toward ethanol compared to other alcohol like 2- propanol, aromatic hydrocarbon like benzene and xylene and ketone like acetone (Fig.3.8(c)). High dissociation energy, poor acidity, larger molecular size, different sticking coefficent were the reasons of poor sensitivity of the sensor toward these other volatile organic compounds (except ethanol) at 100 ppm of concentration at 150 ℃ [41-43].

3.2.5 Role of oxygen vacancy modulation in ethanol sensing

Self-doping, similar to oxygen vacancy (V_O) in metal oxide (MO) semiconductor, influences the gas/vapor sensing performance significantly. In case of microstructure MO, only the surface takes part in gas sensing whereas surface and bulk both contribute in sensing in case of nanostructure metal oxide. So, the tuning of overall (surface and bulk) doping level is important in nanoscale MO to enhance the gas sensing performance.

Donor type dopants like V_O can increase the gas interaction sites or free dangling bond on MO surface that enhance the gas sensing performance due the dissociative adsorption of gas/VOC molecules. Long chain organic molecules are dissociated easily to the oxygen vacancy sites and adsorbed to the free interaction spots. Also, the large number of interaction sites enhance the surface adsorption possibilities of gases/VOCs even at very low temperature increasing the overall sensitivity of the sensor.

However, the increment of V_O has undoubtable advantage to enhance the sensitivity of a gas sensor. As per the microscopic characterizations, morphology of all the four TiO_2 nanotubes were unchanged after self-doping. But, the spectroscopy characterization confirmed that the V_O defect was increased significantly for S_2, S_1 and S_3 samples. As per the above discussion, all the three sensors exhibited very high sensitivity which was maximum for the S_2 and S_1. To get a general view about the effect of donor doping (V_O) on gas sensitivity of a 1-D nanomaterials like TiO_2 nanotubes, the following expression are developed with the help of Fig. 3.9. A schematic of a cross section of nanotube wall (25 to 45 nm in Fig. 2.1) is considered in Fig. 3.9 where surface and core region are indicated separately. Based on the synthesis mechanism of TiO_2 nanotubes by anodic oxidation, core doping is higher than the surface

doping i.e. core carrier concentration (n_c) is greater than surface carrier concentration (n_s) [44]. In air ambient, due to the surface adsorption of oxygen species (O$^-$, O^{2-} etc.), n_s is reduced further that can be written as $n_c \gg n_s$. A surface potential (ψ_S) must be created due to the gradient of the carrier concentration as shown in Eq.3.1 where k is the Boltzmann's constant, T is the temperature and q is the unit change of electron.

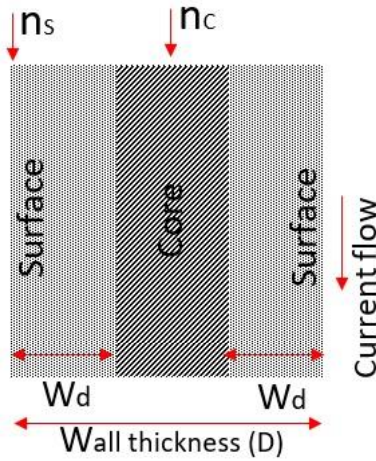$$\psi_s = \frac{kT}{q} ln \left(\frac{n_C}{n_S}\right) \tag{3.1}$$

Fig. 3.9. A two dimensional schematic of the cross sectional view of TiO$_2$ nanotube wall.

Surface depletion width (W_d) can be written as in Eq.3.2 where ε_s (TiO$_2$) and ε_0 are the relative and absolute permittivity [45].

$$W_d = \sqrt{\frac{2\varepsilon_0\varepsilon_s\psi_s}{qn}} \tag{3.2}$$

In Eq.3.2, the effect of bias voltage is considered as negligible as compared to the ψ_s. Also, the average carrier concentration i.e. $n=(n_c+n_s)/2$ is taken in Eq.3.2. As the carrier concentration is more in the core than the surface, the core only take part in current conduction. So, the resistance (R) of a single nanotube between two parallel electrodes (ignoring the contact resistance) can be written by using simple drift equation in Eq.3.3 [18].

$$R = \frac{1}{qn\mu_n}\frac{L}{(D+2r)(D-2W_d)} \tag{3.3}$$

In Eq.3.3, r is the inner radius of the TiO$_2$ nanotubes. Finally, the response magnitude (RM=ΔR/R) expression (Eq.3.4) can be written by considering two different surface carrier concentrations as $n_{s(air)}$ and $n_{s(vapor)}$ as shown in Fig. 3.10. For the reducing gas, $n_{s(vapor)} > n_{s(air)}$.

$$RM = \left[1 - \frac{D - 4\sqrt{\frac{\varepsilon_0 \varepsilon_s kT}{q^2\left(n_c + n_{s(air)}\right)} ln\left(\frac{n_c}{n_{s(air)}}\right)}}{D - 4\sqrt{\frac{\varepsilon_0 \varepsilon_s kT}{q^2\left(n_c + n_{s(vapor)}\right)} ln\left(\frac{n_c}{n_{s(vapor)}}\right)}} \right] \times 100 \qquad (3.4)$$

Eq.3.4 depicts an estimate of response magnitude with tuneable doping level as well as electron concentration in core and surface of the nanotube sensor. The expression says that very high doping in the core of the nanoscale MO semiconductor is responsible for reducing the overall sensitivity. As the oxygen vacancy near the surface enhances the binding interactions of targeted gas/vapor molecules, the increase of self-doping from surface to core can be considered as in favour of better sensitivity.

3.3 Undoped p-type TiO$_2$ nanoparticles

3.3.1 Synthesis

The procedure to synthesize the TiO$_2$ nanoparticles has been described in detail in section 2.3.1 of chapter 2.
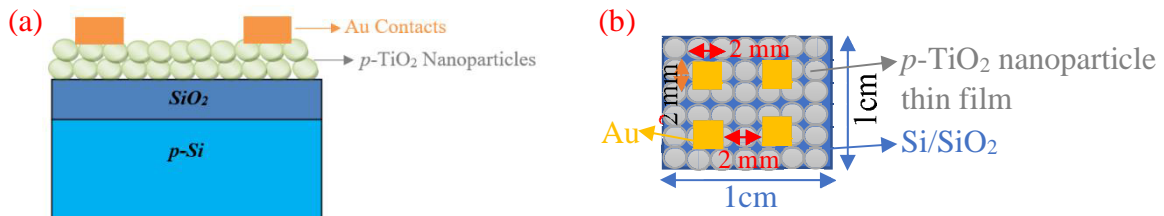
3.3.2 Device fabrication

Fig. 3.10. Planar sensor device structure with dimensions, (a) side view, and (b) top view.

Boron-doped, ~500 µm thick <100> SiO$_2$/Si wafer having SiO$_2$ thickness of 90 nm was used as the substrate where resistivity of Si was 0.001-0.005 Ω-cm. Undoped TiO$_2$ nanoparticles were then deposited on a cleaned SiO$_2$/Si wafer (5 mm × 5 mm) by dip coating technique (Appex Instruments: Xdip-SV-1). All the samples were subsequently kept for annealing at 250 °C for 5 hours.

Similarly, the sample was enfolded in an aluminium mask having four openings of 2 mm × 2 mm each for top electrode formation, separated by a distance of 2 mm. Au was deposited using electron beam deposition technique. The Au deposited with thickness of 100 nm on the sample.
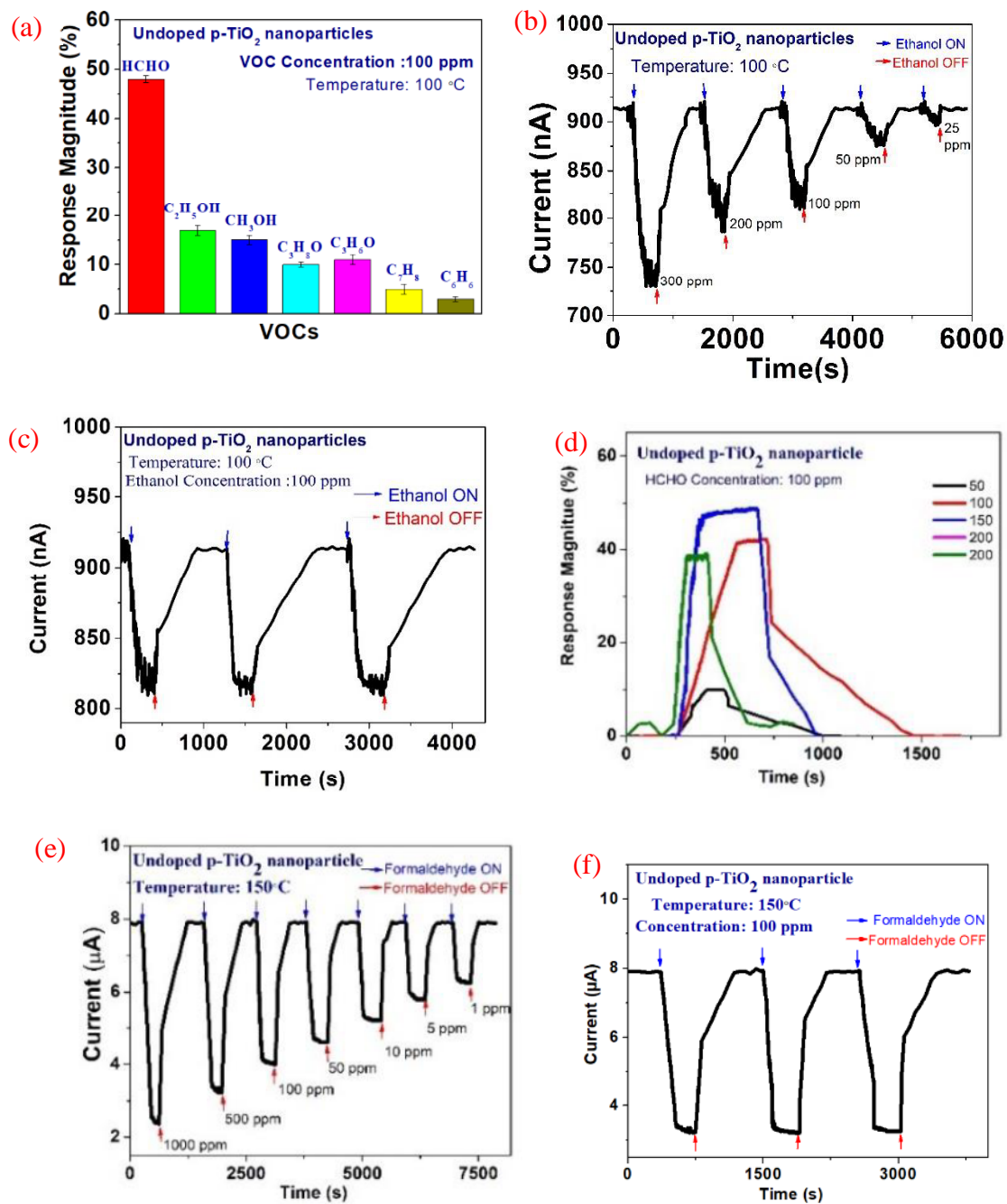
3. 3.2 VOC sensing

Fig. 3.11. Sensing performance of pure TiO$_2$ nanoparticle sensor (S$_1$) (a) Response magnitude to 100 ppm of different VOCs (Formaldehyde, Ethanol, Methanol, Acetone and Toluene) at 100°C, (b) transient behaviour (25 to 300 ppm) towards ethanol at 100 °C, (c) Repeated cycles in exposure to 100 ppm of ethanol at 100 °C, (d) resistive response magnitude at different temperatures (50 °C, 100 °C, 150 °C and 200 °C) in exposure to 100 ppm formaldehyde. (e) transient behaviour (1 to 1000 ppm) towards formaldehyde at 150 °C, (c) Repeated cycles in exposure to formaldehyde at 150 °C.

The TiO$_2$ nanoparticles sensor was placed inside a closed and scaled glass chamber of volume 450 ml with gas inlet, outlet and electrical connections facilities. The glass chamber was positioned inside a heating mantle to vary the temperature from 50 ℃ to 200 ℃. The VOC sensor setup as depicted in Fig. 3.5 is used for sensing application.

TiO$_2$ nanoparticles based planar structure device was first subjected to different groups of VOCs -alcohol (methanol, ethanol and propanol), aldehyde (formaldehyde), ketone (acetone) and aromatic hydrocarbon (benzene and toluene) Fig. 3.11(a). Undoped TiO$_2$ nanoparticles showed the highest response magnitude towards formaldehyde (40%) and then moderate response magnitude towards ethanol (17 %) and methanol (15 %).

The transient response of undoped TiO$_2$ nanoparticle sensor within the ethanol concentration range of 25 ppm to 300 ppm were tested at 100°C and represented in Fig. 3.11(b). TiO$_2$ nanoparticles sensor depicted a stable nature that was confirmed from the repeated cycles taken in exposure to 100 ppm of ethanol at 100 ℃ (Fig. 3.11(c)). Current was decreased in the exposure of reducing vapor ethanol for all the sensors confirming the hole majority in S$_1$. Pure TiO$_2$ NPs (S$_1$) in current study exhibited p-type conductivity due to the availability of excess oxygen that declined the oxygen vacancy (V$_O$) significantly. Therefore, the number of holes contributed by the titanium vacancy (V$_{Ti}$) became greater than the number of electrons donated by the V$_O$ and the current conduction was started through hole in the TiO$_2$ NPs. TiO$_2$ nanoparticle sensor was examined at four different temperatures (50 ℃, 100 ℃ 150 ℃ 200 ℃) in exposure to 100 ppm of formaldehyde. Highest response magnitude was obtained at 150 ℃ towards 100 ppm formaldehyde. Therefore, 150 ℃ was considered as the optimized temperature for formaldehyde sensing. The undoped TiO$_2$ nanoparticles sensor was tested for formaldehyde vapours concentration range from 1000 ppm to 1 ppm at 150 ℃ (Fig. 3.11(e)). Detection down till 1 ppm was achieved as TiO$_2$ nanoparticles sensor was more sensitivity towards formaldehyde. Repeated cycles were performed for 100 ppm of formaldehyde at 150 ℃ (Fig. 3.11(f)).

3.3.3 Sensing mechanism

VOC sensing in TiO$_2$ nanoparticles is principally controlled by the intergranular junctions between two adjacent p-TiO$_2$ nanoparticles as shown in Fig. 3.12. Due to surface adsorption of oxygen species (O$_2^-$, O$^-$, O^{2-}) in air, free electron concentration is reduced and holes are accumulated forming a built-in-potential (qV$_b$) to the surface of the p-TiO$_2$ NPs as shown in the EB diagram in Fig. 3.12.

Reducing gas/vapor (or VOC) reacts with adsorbed oxygen species on the surface of TiO_2 NPs and release of free electron (or accept hole) lowering the built-in-potential as well the thickness of hole accumulation region as shown in Fig. 3.12 [46]. If, I_0 is considered as the current in flat band condition (inert ambient), current in air or reducing ambient can be estimated as a function of built-in-potential as shown in Eq.3.5
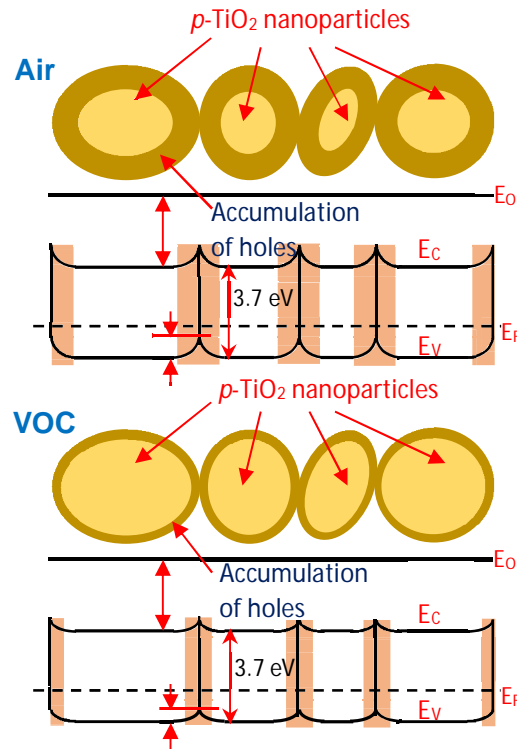

Fig. 3.12. Intergranular junctions between p-TiO_2 NPs with hole accumulation at the surface of nanoparticles in air and VOC ambient.

$$I_{air/VOC} = I_0 exp\left(\frac{qV_{b(air/VOC)}}{kT}\right)$$ (3.5)

Where k is the Boltzmann's constant and T is the temperature [47]. So, the sensor response (S_T) in VOC ambient due to the intergranular junctions between p-TiO_2 NPs can be considered as in Eq.3.6

$$S_G \approx exp\left[\frac{q(V_{b(air)} - V_{b(VOC)})}{kT}\right] \times 100$$ (3.6)

3.4 Conclusions

Highly ordered TiO_2 nanotube was synthesized by electrochemical anodization first and then reduced by (i) cathodic polarization with -1 V and -1.5 V constant potential for few seconds and (ii) chemical reduction by using hydrazine hydrate treatment at 85°C and 115°C. Total five samples; one as-grown (S_0), two cathodic reduction (S_1 and S_2) and two chemical reduction (S_3

and S_4) sample were considered to study the self-doping effect on VOC sensing performance. VOC sensing performance of all the sensors was then tested under 100 ppm of ethanol in the air in the temperature range of 50°C to 200°C. As per the oxygen vacancy level, maximum sensitivity was observed for S_2 and S_1 and gradually decreased for S_3, S_0 and S_4. Almost 60%, 71%, 90 % and 99.5% of response magnitude were recorded for S_2 sample at 50°C, 100°C, 150°C and 200°C respectively. Though the response magnitude was moderate (76% at 150°C), owing to the fastest response (155 s) and recovery time (779 s), S_3 sensor was considered as the best performing sensor.

Undoped p-type TiO_2 nanoparticles prepared via sol-gel method were fabricated in planar device structure. Planar structured undoped p-type TiO_2 nanoparticles sensor depicted high response magnitude of 48 % towards 100 ppm of formaldehyde at 100 ℃. Undoped p-type TiO_2 nanoparticles sensor also depicted a good response magnitude to 100 ppm of ethanol at 100 ℃. The p-type conductivity and VOC sensing mechanism is principally controlled by the intergranular junctions two adjacent TiO_2 nanoparticles.

Nanocarbons have extensively been used to functionalize other nanostructured materials to develop next generation solid state gas sensors with enhanced structural, electrical and chemical properties. Also, the low manufacturing cost, non-toxic nature and minimal defects in the structure have made nanocarbons mostly studied and applied nanomaterial in nanotechnology. Nanocomposites of carbon nanostructures have been extensively scrutinized due to their commendable compatibility, firmness and high versatility In an effort to achieve a high sensitivity in the detection of volatile organic compounds (VOCs), heterojunction of carbon nanostructures (CNT, graphene or graphene oxide and fullerene) with different metal oxides like TiO_2, SnO_2, ZnO, Cu_2O etc. can be synthesized which exhibit excellent properties that are better than sensors fabricated using pure nanocarbon and pure metal oxides.

References

1. K.S. Novoselov, D. Jiang, F. Schedin, T. J. Booth, V. V. Khotkevich, S. V. Morozov, A. K. Geim, Two-dimensional atomic crystals, Proceedings of the National Academy of Sciences 102 30 (2005) 10451-10453.
2. T. Yang, Y. Liu, H. Wang, Y. Duo, B. Zhang, Y. Ge, H. Zhang, W. Chen, Recent advances in 0-D nanostructure-functionalized low-dimensional nanomaterials for chemiresistive gas sensors, Journal of Materials Chemistry C 8 22 (2020) 7272-7299.

3. P. V. Kamat, TiO$_2$ nanostructures: recent physical chemistry advances, (2012) 11849-11851.

4. H. Ji, W. Zeng, Y. Li, Gas sensing mechanisms of metal oxide semiconductors: a focus review, Nanoscale 11 47 (2019) 22664-22684.

5. Z. Li, H. Li, Z. Wu, M. Wang, J. Luo, H. Torun, P. A. Hu, C. Yang, M. Grundmann, X. Liu, Y. Q. Fu, Advances in designs and mechanisms of semiconducting metal oxide nanostructures for high-precision gas sensors operated at room temperature, Materials Horizons 6 3 (2019) 470-506.

6. Z. Wen, L. Tian-mo, Hydrogen sensing characteristics and mechanism of nanosize TiO$_2$ dope with metallic ions, Physical B: Condensed Matter 405 2 (2010) 564-568.

7. Q. Wang, Y. Z. Pan, S. S. Huang, S. T. Ren, P. Li, J. J. Li, Resistive and capacitive response of nitrogen-doped TiO$_2$ nanotubes film humidity sensor, Nanotechnology 22 2 (2010) 025501.

8. Y. C. Nah, I. Paramasivam, P. Schmuki, Doped TiO$_2$ and TiO$_2$ nanotubes: synthesis and applications, ChemPhysChem 11 13 (2010) 2698-2713.

9. J. Moon, J. A. Park, S. J. Lee, T. Zyung, I. D. Kim, Pd-doped TiO$_2$ nanofiber networks for gas sensor applications, Sensors and Actuators B: Chemical 149 1 (2010) 301-305.

10. Y. Fan, H. T. Lu, J. H. Liu, C. P. Yang, Q. S. Jing, Y. X. Zhang, X. K. Yang, K. J. Huang, Hydrothermal preparation and electrochemical sensing properties of TiO$_2$–graphene nanocomposite, Colloids and Surfaces B: Biointerfaces 83 1 (2011) 78-82.

11. F. Mendoza, D.M. Hernández, V. Makarov, E. Febus, B. R. Weiner, Gerardo Morell, Room temperature gas sensor based on tin dioxide-carbon nanotubes composite films, Sensors and Actuators B: Chemical 190 (2014) 227-233.

12. Y. Wei, C. Chen, G. Yuan, S. Gao, SnO$_2$ nanocrystals with abundant oxygen vacancies: preparation and room temperature NO$_2$ sensing, Journal of Alloys and compounds 681 (2016) 43-49.

13. D. Wang, J. Sun, X. Cao, Y. Zhu, Q. Wang, G. Wang, Y. Han, G. Lu, G. Pang, S. Feng, High-performance gas sensing achieved by mesoporous tungsten oxide mesocrystals with increased oxygen vacancies, Journal of Materials Chemistry A 1 30 (2013) 8653-8657.

14. C. Zou, F. Liang, S. Xue, Synthesis and oxygen vacancy related NO$_2$ gas sensing properties of ZnO: Co nanorods arrays gown by a hydrothermal method, Applied Surface Science 353 (2015) 1061-1069.

15. J. Wu, Q. Huang, D. Zeng, S. Zhang, L. Yang, D. Xia, Z. Xiong, C. Xie, Al-doping induced formation of oxygen-vacancy for enhancing gas-sensing properties of SnO_2 NTs by electrospinning, Sensors and Actuators B: Chemical 198 (2014) 62-69.

16. A. Hazra, B. Bhowmik, K. Dutta, P. P. Chattopadhyay, P. Bhattacharyya, Stoichiometry, length, and wall thickness optimization of TiO_2 nanotube array for efficient alcohol sensing, ACS applied materials & interfaces 7 18 (2015) 9336-9348.

17. A. Hazra, K. Dutta, B. Bhowmik, P. P. Chattopadhyay, P. Bhattacharyya, Room temperature alcohol sensing by oxygen vacancy controlled TiO_2 nanotube array, Applied Physics Letters 105 8 (2014) 081604.

18. L. Yu, F. Guo, S. Liu, B. Yang, Y. Jiang, L. Qi, X. Fan, Both oxygen vacancies defects and porosity facilitated NO_2 gas sensing response in 2D ZnO nanowalls at room temperature, Journal of Alloys and Compounds 682 (2016) 352-356.

19. A. S. Barnard, L. A. Curtiss, Prediction of TiO_2 nanoparticle phase and shape transitions controlled by surface chemistry, Nano letters 5 7 (2005) 1261-1266.

20. A. Teleki, S. E. Pratsinis, K. Kalyanasundaram, P. I. Gouma, Sensing of organic vapours by flame-made TiO_2 nanoparticles, Sensors and actuators B: chemical 119 2 (2006) 683-690.

21. M. M. Arafat, A. S. M. A. Haseeb, S. A. Akbar, A selective ultrahigh responding high temperature ethanol sensor using TiO_2 nanoparticles Sensors 14 8 (2014) 13613-13627.

22. R. Rella, J. Spadavecchia, M. G. Manera, S. Capone, A. Taurino, M. Martino, A. P. Caricato, T. Tunno, Acetone and ethanol solid-state gas sensors based on TiO_2 nanoparticles thin film deposited by matrix assisted pulsed laser evaporation, Sensors and Actuators B: Chemical 127 2 (2007) 426-431.

23. R. Pandeeswari, R. K. Karn, B. G. Jeyaprakash, Ethanol sensing behaviour of sol–gel dip-coated TiO_2 thin films, Sensors and Actuators B: Chemical 194 (2014) 470-477.

24. H. Pelouchova, P. Janda, J. Weber, L. Kavan, Charge transfer reductive doping of single crystal TiO_2 anatase, Journal of Electroanalytical Chemistry 566 1 (2004) 73-83.

25. H. Zhou, Y. Zhang, Electrochemically self-doped TiO_2 nanotube arrays for supercapacitors, The Journal of Physical Chemistry *C* 118 11 (2014) 5626-5636.

26. J. M. Macak, B. G. Gong, M. Hueppe, P. Schmuki, Filling of TiO_2 Nanotubes by Self-Doping and Electrodeposition, Advanced Materials 19 19 (2007) 3027-3031.

27. Q. Shi, R. Lu, K. Jin, Z. Zhang, D. Zhao, Simple and eco-friendly reduction of nitroarenes to the corresponding aromatic amines using polymer-supported hydrazine hydrate over iron oxide hydroxide catalyst, Green Chemistry 8 10 (2006) 868-870.

28. D. M. Littrell, D. H. Bowers, B. J. Tatarchuk, Hydrazine reduction of transition-metal oxides, Journal of the Chemical Society, Faraday Transactions 1: Physical Chemistry in Condensed Phases 83 11 (1987) 3271-3282.

29. V. Andal, G. Buvaneswari, Effect of reducing agents in the conversion of Cu_2O nanocolloid to Cu nanocolloid, Engineering Science and Technology, an International Journal 20 1 (2017) 340-344.

30. T. Akita, M. Okumura, K. Tanaka, K. Ohkuma, M. Kohyama, T. Koyanagi, M. Date, S. Tsubota, M. Haruta, Transmission electron microscopy observation of the structure of TiO_2 nanotube and Au/TiO_2 nanotube catalyst, Surface and Interface Analysis: An International Journal devoted to the development and application of techniques for the analysis of surfaces, interfaces and thin films 37 2 (2005) 265-269.

31. L. Z. Liu, W. Xu, X. L. Wu, Y. Y. Zhang, T. H. Chen, P. K. Chu Liu, Electronic states and photoluminescence of TiO_2 nanotubes with adsorbed surface oxygen, Applied Physics Letters 100 12 (2012) 121904.

32. K. Iijima, M. Goto, S. Enomoto, H. Kunugita, K. Ema, M. Tsukamoto, N. Ichikawa, H. Sakama, Influence of oxygen vacancies on optical properties of anatase TiO_2 thin films, Journal of Luminescence 128 5-6 (2008) 911-913.

33. C. Mercado, Z. Seeley, A. Bandyopadhyay, S. Bose, J. L. McHale, Photoluminescence of dense nanocrystalline titanium dioxide thin films: effect of doping and thickness and relation to gas sensing, ACS applied materials & interfaces 3 7 (2011) 2281-2288.

34. M. Yang, W. Liu, J. L. Sun, J. L. Zhu, High magnetic field annealing effect on visible photoluminescence enhancement of TiO_2 nanotube arrays, Applied Physics Letters 100 4 (2012) 043106.

35. B. Choudhury, A. Choudhury, Luminescence characteristics of cobalt doped TiO_2 nanoparticles, Journal of luminescence 132, 1 (2012) 178-184.

36. H. Tang, H. Berger, P. E. Schmid, F. Levy, G. Burri, Photoluminescence in TiO_2 anatase single crystals, Solid State Communications 87 9 (1993) 847-850.

37. J.C. Parker, R. W. Siegel, Calibration of the Raman spectrum to the oxygen stoichiometry of nanophase TiO_2, Applied Physics Letters 57 9 (1990) 943-945.

38. X. Pan, M. Q. Yang, X. Fu, N. Zhang, and Y. J. Xu, Defective TiO_2 with oxygen vacancies: synthesis, properties and photocatalytic applications, *Nanoscale* 5 9 (2013) 3601-3614.

39. D. Bersani, P. P. Lottici, X. Z. Ding, Phonon confinement effects in the Raman scattering by TiO_2 nanocrystals, Applied Physics Letters 72 1 (1998) 73-75.

40. M. Scepanovic, M. Grujic-Brojcin, Z. Dohcevic-Mitrovic, Z. V. Popovic, Effects of confinement, strain and nonstoichiometry on Raman spectra of anatase TiO_2 nanopowders, In *Materials Science Forum,* 518 Trans Tech Publications Ltd (2006) 101-106.

41. M. Orzol, I. Martin, J. Kocisek, I. Dabkowska, J. Langer, E. Illenberger, Bond and site selectivity in dissociative electron attachment to gas phase and condensed phase ethanol and trifluoroethanol, Physical chemistry chemical physics 9 26 (2007) 3424-3431.

42. D.S. Slaughter, D.J. Haxton, H. Adaniya, T. Weber, T.N. Rescigno, C.W. McCurdy, A. Belkacem, Ion-momentum imaging of resonant dissociative-electron-attachment dynamics in methanol, Physical Review A 87 5 (2013) 052711.

43. M. Lepage, M. Michaud, L. Sanche, Low-energy electron scattering cross section for the production of CO within condensed acetone, The Journal of Chemical Physics 113 9 (2000) 3602-3608.

44. A. Hazra, B. Bhowmik, K. Dutta, V. Manjuladevi, R. K. Gupta, P. P. Chattopadhyay, P. Bhattacharyya, Formation mechanism of anodically grown free-standing TiO_2 nanotube array under the influence of mixed electrolytes, Science of Advanced Materials 6 4 (2014) 714-719.

45. S. M. Sze, K. N. Kwok, Physics of semiconductor devices, John wiley & sons (2021).

46. A. Hazra, B. Bhowmik, K. Dutta, V. Manjuladevi, R. K. Gupta, P. Bhattacharyya, Low temperature methanol sensing by p-type nano-titania: Correlation with defects states and Schottky barrier model, IEEE Transactions on Nanotechnology 14 (2014) 187-195.

47. A. Hazra, P. Bhattacharyya, Tailoring of the gas sensing performance of TiO_2 nanotubes by 1-D vertical electron transport technique, IEEE Transactions on Electron Devices, 61 (2014) 3483-3489.